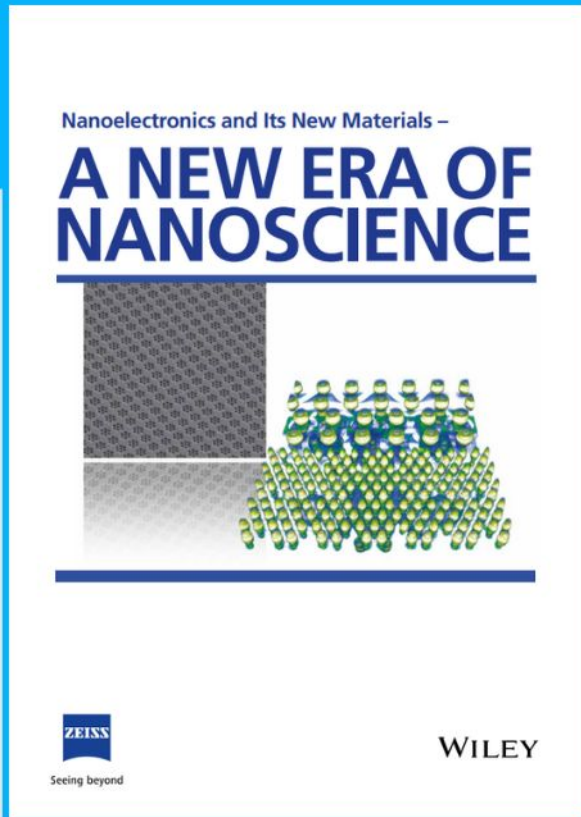




Nanoelectronics and Its New Materials – A NEW ERA OF NANOSCIENCE



Discover the recent advances in electronics research and fundamental nanoscience.

Nanotechnology has become the driving force behind breakthroughs in engineering, materials science, physics, chemistry, and biological sciences. In this compendium, we delve into a wide range of novel applications that highlight recent advances in electronics research and fundamental nanoscience. From surface analysis and defect detection to tailored optical functionality and transparent nanowire electrodes, this eBook covers key topics that will revolutionize the future of electronics.

To get your hands on this valuable resource and unleash the power of nanotechnology, simply download the eBook now. Stay ahead of the curve and embrace the future of electronics with nanoscience as your guide.



Seeing beyond

WILEY

Ultra-Stretchable Spiral Hybrid Conductive Fiber with 500%-Strain Electric Stability and Deformation-Independent Linear Temperature Response

Jianpeng Wu, Min Sang, Jingyi Zhang, Yuxi Sun, Xinyi Wang, Junshuo Zhang, Haoming Pang, Tianzhi Luo, Shaoshan Pan, Shouhu Xuan,* and Xinglong Gong*

Stretchable configuration occupies priority in devising flexible conductors used in intelligent electronics and implantable sensors. While most conductive configurations cannot suppress electrical variations against extreme deformation and ignore inherent material characteristics. Herein, a spiral hybrid conductive fiber (SHCF) composed of aramid polymeric matrix and silver nanowires (AgNWs) coating is fabricated through shaping and dipping processes. The homochiral coiled configuration mimicked by plant tendrils not only enables its high elongation (958%), but also generates a superior deformation-insensitive effect to existing stretchable conductors. The resistance of SHCF maintains remarkable stability against extreme strain (500%), impact damage, air exposure (90 days), and cyclic bending (150 000 times). Moreover, the thermal-induced densification of AgNWs on SHCF achieves precise and linear temperature response toward a broad range (−20 to 100 °C). Its sensitivity further manifests high independence to tensile strain (0%–500%), allowing for flexible temperature monitoring of curved objects. Such unique strain-tolerant electrical stability and thermosensation hold broad prospects for SHCF in loss-less power transferring and expeditious thermal analysis.

tolerant geometries.^[4,5] With increasing demand for steady signal outputs under tensile state, recent researches on conductor fabrications mainly focus on the design of multiscale configurations based on highly conductive composites to acquire strain-insensitive structural features. Therefore, by means of a series of manufacturing strategies, including Kirigami-cutting on conductive nanopapers,^[6,7] buckle-delaminating rigid circuits,^[8] as well as self-adaptive water-to-net interacting,^[9] the resistance changes in flexible conductors during stretching have been obviously reduced. However, when it comes to some extreme occasions, especially for large strain (above 200%), high-speed impact damage, and long-term fatigue test (over 10 000 cycles), these configurations always fail to guarantee satisfactory electrical stability. This intractable deficiency is ascribed to low structural resilience along with poor

material robustness, which may cause serious signal distortion during information transmission.^[10,11]

In addition, a majority of flexible conductors are aimed to eliminate the resistance variations induced by local strain via stretchable configurations, while rare of them consider further expansions on the deformation-independent physical monitoring.^[12,13] Since the interference on electrical performances from mechanical loading can be effectively suppressed by these configurations, intrinsic material functions (e.g., thermo-response or gas-sensation) have the potential to operate normally at deformable regions. For example, through minimizing the true strain applied to base material, the Kirigami structure has been proven to greatly attenuate the cross-sensitivity of external stretching to temperature sensing device, which enables a highly stable monitoring capacity even at 100% tensile strain.^[14] The circuitous serpentine architecture in an epidermal sensor also avoids substantial changes in temperature sensitivity under 30% strain due to its slow structural extension.^[13] Therefore, more attention should be paid to the electrical robustness and stretchable features of flexible conductors to fulfill the multifunctional requirements of next-generation electronic devices.


In nature, some plants such as cucumbers and towel grounds yield tendril filament helices from stems or leaves to

1. Introduction

Flexible conductors with robust electrical stability against extreme deformation are rapidly gaining popularity in various applications such as transmission electrodes, wearable sensing, and human-machine interactions.^[1–3] In general, high-performance electronic products derived from flexible conductors deeply rely on the stretchability of matrices, low resistivity of conductive components, and morphing-

J. Wu, M. Sang, J. Zhang, Y. Sun, X. Wang, J. Zhang, H. Pang, T. Luo, S. Pan, S. Xuan, X. Gong
CAS Key Laboratory of Mechanical Behavior and Design of Materials
Department of Modern Mechanics
University of Science and Technology of China (USTC)
Hefei, Anhui 230027, P. R. China
E-mail: xuansh@ustc.edu.cn; gongxl@ustc.edu.cn

S. Xuan, X. Gong
State Key Laboratory of Fire Science
University of Science and Technology of China (USTC)
Hefei, Anhui 230026, P. R. China

 The ORCID identification number(s) for the author(s) of this article can be found under <https://doi.org/10.1002/sml.202207454>.

DOI: 10.1002/sml.202207454

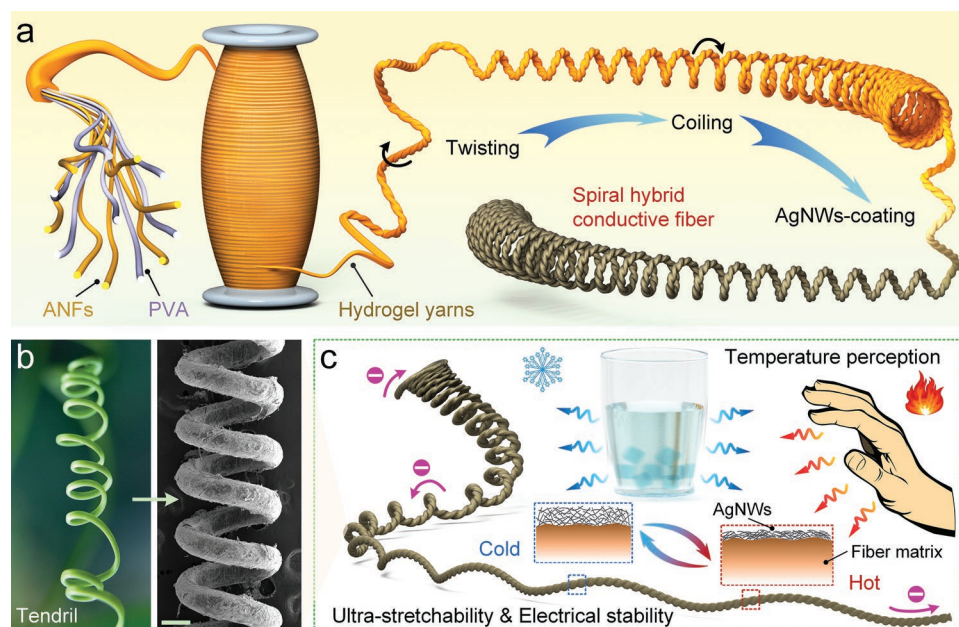


Figure 1. Fabrication and features of SHCF. a) Schematic illustration of the preparation of SHCF through twisting, coiling, and AgNWs-coating the ANFs/PVA hydrogel yarns. b) Comparison of cucumber tendril and the homochiral coiled structure of SHCF. Scale bar, 300 μm . c) Scheme for the high stretchability, strain-insensitive electrical stability, and temperature perception of SHCF.

climb anchored supports for absorbing sunlight.^[15] Through twining surrounding supports, the chiral structure of tendril helices provides an elastic constraint for plants to resist destruction in harsh climates. In this regard, the tendril-like biological configurations have offered multiple implications in artificial muscles, soft robotics, and strain sensors due to their outstanding stretchability.^[16–18] Besides, by virtue of the potential length hiding in helical structure, tendril-like configurations are capable of transforming uniaxial stretch into gentle filament uncoiling, thus effectively retarding strain growth on base materials. Such a unique deformation mechanism not only achieves higher elongation (above 1000%) of structural devices in comparison to that in Kirigami and buckling configurations,^[18] but also minimizes strain interference on innate material characteristics. Nonetheless, the strain-insensitive feature derived from the uncoiling motion of helical structure has not yet been well excavated. Therefore, as for flexible conductors, an accessible approach to obtain substantive improvement in electrical stability against extreme deformation lies in the construction of stretchable tendril-like springs. Furthermore, the approach is expected to ensure the normal operation of intrinsic material functions even suffering mechanical strain.

Aramid nanofibers (ANFs), the nanoscale derivatives of bulk Kevlar fabrics, possess outstanding specific strength and broad temperature resistance owing to the abundant rigid benzene rings.^[19,20] Through deprotonation in alkali and polar solvents, microfibrils of ANFs have been successfully assembled into 1D spun yarns, strong nanofilms, as well as porous aerogels.^[21–24] However, the demerits of low elongation and high stiffness severely limit their further processability toward stretchable configurations. In contrast, polyvinyl alcohol (PVA), which is widely used in organic hydrogels as a toughening component, exhibits exceptional flexibility at large tensile strain.^[25] However, the

microstructures and nanocrystalline domains of PVA are easy to be destroyed at extreme temperatures due to poor thermal stability. Fortunately, strong hydrogen bonding interactions among polar groups have enabled a perfect structural complement between the stiff scaffolds of ANFs and flexible molecular chains of PVA.^[26] Harnessing this synergistic stiffness and toughness, the crosslinked ANFs/PVA is hopeful to be processed into highly distorted tendril-like configuration as the matrix of flexible conductors. Furthermore, silver nanowires (AgNWs) are considered as excellent 1D conductive nanomaterial with a large aspect ratio.^[27] They can be tightly deposited on the surface of aramid polymeric matrix and connect mutually into effective conductive network via simple dip-coating or vacuum filtration.^[28]

In this work, an ultra-stretchable spiral hybrid conductive fiber (SHCF) is devised by mimicking the helical configuration of cucumber tendrils (Figure 1b). Specifically, ANFs/PVA hydrogel yarns are first prepared via a temperature-controlled wet spinning strategy, and then shaped into spiral morphology by twisting-coiling clockwise (Figure 1a), whose surface is further dip-coated with highly conductive AgNWs. Benefiting from the tendril-inspired homochiral coiled microstructure (right side in Figure 1b), SHCF exhibits maximum elongation of 958% yet retains high strength of 130 MPa. The uncoiled motion of spiral morphology produces a significant strain-insensitive feature, which enables SHCF with simultaneous morphing-tolerant electrical stability and temperature response (Figure 1c). In particular, the resistance of SHCF exhibits tiny variation against extreme tensile strain (0%–500%). The thermal-induced stack densification of AgNWs (Figure 1c dashed boxes) further realizes a broad response to environment temperature (–20 to 100 °C). Benefiting from the elimination of strain interference by helical configuration, the temperature sensitivity also remains unchanged even at 500% tensile strain.

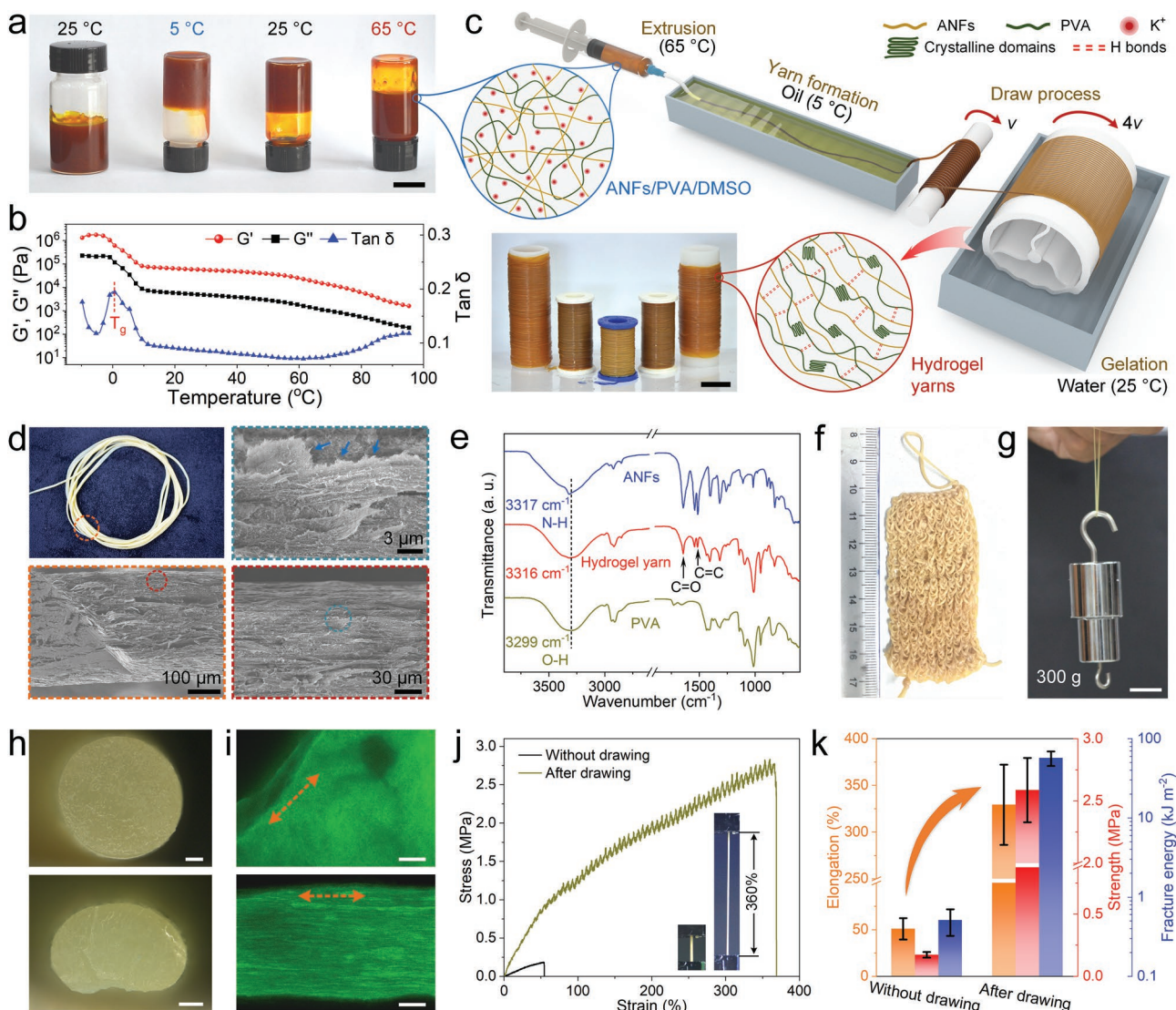


Figure 2. Preparation and characterization of ANFs/PVA hydrogel yarns. a,b) Photographs and temperature-dependent rheological properties of ANFs/PVA/DMSO mixture. Scale bar, 15 mm. G' and G'' were measured using oscillating shear mode with a frequency of 1 Hz at strain of 0.1%. c) Schematic diagram of the wet-spinning process of ANFs/PVA hydrogel yarns. (Inset represents the scalable production of hydrogel yarns. Scale bar, 30 mm) d) SEM images of longitudinal section of the hydrogel yarns. Blue arrows represent the nanofibrils pullout. e) FTIR spectra of ANFs, PVA, and hydrogel yarn. f) Photograph of textile woven with hydrogel yarns. g) Optical image illustrating the favorable strength of hydrogel yarn. Scale bar, 20 mm. h) Optical micrographs of cross-sections of hydrogel yarns with (bottom) and without (top) drawing. Scale bars, 200 μm . i) Confocal images of hydrogel yarns with (bottom) and without (top) drawing. Dash lines represent the yarn forming direction. Scale bars, 20 μm . j) Tensile stress-strain curves of hydrogel yarns with and without drawing. (Insets represent hydrogel yarn with drawing at strains of 0% and 360%) k) Summary of elongation, strength, and fracture energy of hydrogel yarns. Error bars represent standard deviation.

Compared with reported flexible conductors that suffered either costly fabrication procedures or poor stretchability,^[10,29] the versatile SHCF pioneers a facile strategy to achieve robust electrical stability and deformable temperature monitoring.

2. Results and Discussion

2.1. Wet-Spinning of ANFs/PVA Hydrogel Yarns

The dark red ANFs dispersion (2 wt.%, Figure S1a, Supporting Information) was obtained by dissolving para-aramid fabrics in

DMSO (dimethyl sulfoxide) along with an equivalent amount of KOH (potassium hydroxide), where KOH provided alkaline condition to deprotonate the nanofibers.^[19] Then, ANFs/DMSO was homogeneously mixed with PVA dispersion (10 wt.%, Figure S1b, Supporting Information) at a mass ratio of 1:1. The resultant ANFs/PVA/DMSO mixture retained original red color of ANFs/DMSO but exhibited obviously temperature-dependent viscoelastic feature (Figure 2a). Because of the high viscosity of employed PVA (54–66 mPa s), the mixture remained at the bottom of inverted bottle at 5–25 °C and became flowable at 65 °C. Figure 2b displays the corresponding rheological property. The storage modulus (G') of ANFs/PVA/DMSO

mixture maintained a high level of 1.03–1.77 GPa at the initial loading stage of -10 to 0 °C. But it dramatically dropped to 74 MPa as the temperature increased to 10 °C. The glass transition temperature (T_g) occurred at 0 °C, in which this mixture showed a phase transition from frozen state to viscoelastic state. When the temperature was further elevated, both G' and G'' (loss modulus) decreased continuously. The mixture gradually changed from viscoelastic dominant to fluid dominant and underwent a second phase transition at ≈ 50 °C (Figure S2a, Supporting Information), where PVA molecular chains possessed high mobility due to the weak entanglement with ANFs (Figure 2c blue circle). The decreased viscosity with shear rate reflected a strong shear thinning effect (Figure S2b, Supporting Information), which was beneficial for the mixture to flow across the injection orifice smoothly. Besides, the initial viscosity descended gradually with increasing temperature from 50 to 75 °C owing to the improved molecular chain mobility.

Given the distinctive rheological performance, a temperature-controlled wet-spinning strategy was proposed here to prepare ANFs/PVA hydrogel yarns for the first time (Figure 2c). Specifically, ANFs/PVA/DMSO mixture was heated to ≈ 65 °C to form low-viscosity spinning dopes and then extruded steadily from a round nozzle (18 G). The fresh dopes further extended along a Teflon tube (internal diameter, 1.2 mm) connected with an oil sink to form slender yarns. To maintain the slender shape, the oil sink provided a low bath temperature (≈ 5 °C) to rapidly cool the extruded dopes into viscoelastic yarns (Movie S1, Supporting Information). Note that the extrusion process had a moderate contribution to the orienting of ANFs/PVA microfibrils and toughening of final hydrogel yarns (as discussed later). Therefore, a yarn-drawing treatment was utilized to further promote the aggregation and self-assembly level of ANFs/PVA microfibrils.^[26] Specifically, the extruded dopes were collected and stretched to four times of the original length by a pair of synchronous rollers with a diameter ratio of 1:4 (Figure 2c). After gelation and solvent removal (DMSO and oil) in water, reprotonation of ANFs, crystallization of PVA chains, and hydrogen bond crosslinking among ANFs/PVA occurred simultaneously (Figure 2c red circle and Figure S1c, Supporting Information) in the extruded dopes, which resulted in the scalable production of highly oriented and stretchable hydrogel yarns (Figure 2c inset).

The pale-yellow hydrogel yarns presented dense microstructure in the longitudinal section torn along draw direction (Figure 2d orange box) that was composed of massively aligned ANFs/PVA microfibrils (Figure 2d red box). Benefiting from the hydrogen bond crosslinks, the loose nanofiber networks of ANFs were toughened by tightly wrapping and bundling of PVA colloids (Figure S3, Supporting Information), which in turn served as rigid scaffolds to transfer loading throughout the whole matrix.^[30] Extensive nanofibrils pullouts observed at the tear section (Figure 2d blue arrows) were expected to enhance the plastic deformation and energy dissipation before tensile fracture. Furthermore, FTIR (Fourier transform infrared) spectra of hydrogel yarns revealed the stretching vibration peaks of C=O (1644 cm^{-1}) and C=C (1515 cm^{-1}) groups originated from ANFs (Figure 2e black arrows).^[31] The O–H stretching vibration at 3299 cm^{-1} of PVA shifted to a higher wavenumber of 3316 cm^{-1} in hydrogel yarns, confirming hydrogen bonding

between O–H of PVA and N–H of ANFs (Figure S1c, Supporting Information).^[32] In short, the intermolecular crosslinks along with oriented microfibrils endowed hydrogel yarns with exceptional flexibility and strength, allowing them to be woven into a textile or lift 300 g weights without breakage (Figure 2f,g).

It is worth noting that the favorable mechanical strength of the hydrogel yarns could be greatly attributed to the draw-induced microfibrils' orientation during wet-spinning process (Figure 2C). Herein, hydrogel yarns without drawing were prepared as a control. Optical micrographs identified the elliptical cross-section and thinned longitudinal profile (Figure 2h and Figure S4, Supporting Information) of hydrogel yarns after drawing due to the stretch and wrap actions of rotating rollers (see details in "Experimental" section). The fibrous micro-morphologies characterized by confocal stained images further revealed the long-range hierarchical structure along draw direction (Figure 2i bottom and Figure S5c, Supporting Information), which was in sharp contrast to the homogeneous interior of fibers without drawing (Figure 2i top). A magnified view also exhibited the highly aligned microfibrils in densified arrangement (Figure S5d, Supporting Information). As a result, the draw-induced microscopic orientation enabled tremendous reinforcement in the ductility of macroscopic fibers.^[33] As shown in Figure 2j, the elongation at break of hydrogel yarns increased significantly from $50.9 \pm 11.5\%$ to $329.3 \pm 42.9\%$ after draw treatment. Besides, the tensile strength and fracture energy reached 2.6 ± 0.3 MPa and 571 ± 11.9 kJ m^{-2} respectively, which were 15 times and 111 times higher than that of undrawn samples (Figure 2k). Compared with previous PVA-based hydrogels (e.g., polyacrylamide/PVA, glycyrrhiza acid/PVA) and other tough hydrogels (e.g., cellulose, chitin), this hydrogel yarns composed of crosslinked ANFs/PVA exhibited simultaneously high elongation and strength (Figure S6, Supporting Information).

2.2. Preparation and Mechanical Performance of Spiral Hybrid Fiber

High stretchability and super elasticity were desirable for flexible conductors. By virtue of the exceptional toughness (Figure 2k), the hydrogel yarns could be processed into ultra-stretchable matrix through severe twisting and coiling treatments, and finally coated with conductive nanowires (as discussed in next section). Specifically, hydrogel yarn was straightened by tethering both ends, and then twisted clockwise at one side along axial direction with a given density of 1500 turns m^{-1} (Figure 3b, schematic). The twisted hydrogel yarn was further coiled tightly around a mandrel (Φ 0.7 mm) clockwise and annealed at 100 °C for 3 h. After thermally setting the distorted ANFs/PVA microfibrils (Figure S7c, Supporting Information), the obtained spiral hybrid fiber achieved a homochiral coiled microstructure with the same twisting and coiling directions (Figure 3c). In comparison, straight hybrid fibers only annealed at 100 °C exhibited a curved rectangle cross-section retained from the hydrogel yarns (Figure 3a and Figure 2h bottom). Water loss during annealing promoted the aggregation of microfibrils and eliminated internal voids of hydrogel yarns (Figure 2d), leading to obvious volume shrinkage and structural

densification of straight hybrid fibers (Figure S7a, Supporting Information). In contrast, the twisted hybrid fibers exhibited a circular section due to severe self-torsion along axial direction ($1500 \text{ turns m}^{-1}$, Figure 3b). The highly distorted microfibrils were extensively distributed on the fiber surface and formed compact bias interfaces with an angle of 34° (Figure 3b inset and Figure S7b, Supporting Information). Based on the twisted structure, the spiral hybrid fibers after coiling acquired typical spring-like morphology that hid potential fibril length (Figure 3c), which played a crucial role in withstanding large deformation. Moreover, the homogenous distributions of C/N/O (Figure 3d) reflected wide crosslinks between ANFs and PVA in the twisted position (Figure 3c orange circle). Such a simple twisting-coiling method enabled excellent flexibility and large size of spiral hybrid fibers (Figure 3e,f).

Tensile properties of these three fibers were systematically investigated. Compared to hydrogel yarns, both the ultimate strengths of straight hybrid fibers and twisted hybrid fibers improved obviously (233.3 ± 13.3 and $118.8 \pm 20.5 \text{ MPa}$) owing to the microfibrils aggregation during annealing (Figure 3g). While the elongations at break only were $9.0 \pm 2.1\%$ for straight hybrid fibers and $3.9 \pm 1.0\%$ for twisted hybrid fibers. Notably, after coiling the twisted structure, the spiral hybrid fibers achieved ultra-stretchability with maximum elongation of $700.1 \pm 100.5\%$ (Figure 3h). Figure 3k reveals the stepwise tensile process from original length to 800% strain, which contained three distinctive stages: initial uncoiling with linear deformation (0%–100%), uncoiling and gentle microfibrils elongation (100%–700%), and overall fiber elongation (above 700%). Although the ultimate strength declined to $12.9 \pm 1.3 \text{ MPa}$ due to stress concentration in highly distorted microfibrils, the large tensile strain was expected to impart spiral hybrid fibers broad potential in stretchable conductors and artificial muscles.^[33,34] It was worth noting that the extraordinary stretchability also ascribed to twist-induced microfibrils aggregation. In comparison, the hydrogel yarn was directly coiled and annealed to produce the single helical structure (it was named as “untwisted spiral hybrid fiber”, Figure S8a, Supporting Information). Due to the absence of twisting process, it exhibited a thin fiber plate that was prone to be torn under excessive distortion, whose elongation only reached $162.3 \pm 32.3\%$ (Figure S8b, Supporting Information). Besides, the spiral hybrid fibers were proven to have favorable resilience at large deformation. During the consecutive loading-unloading test from 100% to 500% strain (Figure 3i), the maximum stresses increased successively and coincided with the loading trajectory of tensile-broken curve in Figure 3h. The spiral hybrid fibers had a complete elastic range of 0%–200% and kept moderate residual deformations at 400% and 500% (150% and 240%, respectively). Fatigue test at 100% strain further confirmed the long-term elasticity. As shown in Figure 3j insets, the tensile stress maintained 91% of initial value (6.39 MPa) after 100 tensile cycles. Even after 500 cycles, the stress retention was up to 86%, evidencing the sturdy spring geometry of spiral hybrid fibers. Benefiting from the high stretchability and resilience, the spiral hybrid fibers could be processed into various load-bearing devices. For example, a lightweight stretcher composed of six spiral hybrid fibers with total mass of 0.06 g could pull up a suit of weights up to 700 g while maintaining the coiled structures (Figure 3l and Figure S9,

Supporting Information). An elastic net woven by 22 spiral hybrid fibers (Figure 3m) also exhibited extreme elasticity during the buffer process of a raw egg drooped from 10 cm height (Figure 3n and Movie S2, Supporting Information).

2.3. Strain-Insensitive Electrical Stability of SHCF

The spiral hybrid fiber could be further developed into ultra-stretchable conductor through simple dip-coating treatment. Herein, self-prepared AgNWs/ethanol dispersion (silver nanowires, length: 1–3 μm , Figure S10, Supporting Information) was employed to coat the surface of spiral hybrid fiber and then annealed at 60°C . After repeated coating-annealing for 10 times, the obtained SHCF had a slight mass increment (7.91%, Figure S11, Supporting Information). While the surface transformed from pale-yellow to yellow-green with obvious metallic luster (Figure 4a, optical micrographs). SEM images revealed the extensive deposition of AgNWs on the ANFs/PVA matrix (Figure 4b) that connected mutually into a highly conductive path along the coiled scaffold. It exhibited good conductivity ($68.6 \pm 0.6 \Omega \text{ cm}^{-1}$), large-size ($\approx 70 \text{ cm}$), and ultra-stretchability (Figure 4c). As a comparison, the straight hybrid conductive fiber and twisted hybrid conductive fiber were prepared through the identical coating treatment (Figure S12, Supporting Information). The two hybrid conductive fibers retained high ultimate strengths from the pure fibers in Figure 3g, but achieved obvious improvement in elongations ($15.4 \pm 3.8\%$ and $19.7 \pm 9\%$ respectively, Figure 4d inset). It may be attributed to the reduction of internal stress in microfibrils induced by recrystallization during low-temperature annealing at 60°C .^[35] Such a toughening phenomenon appeared in SHCF as well. In Figure 4e, the stress grew linearly with strain at 0%–500%, which was dominated by uncoiling deformation, and then soared to 146.5 MPa at 900% due to the microfibrils stretch. The simultaneously enhanced elongation and strength of SHCF (Figure 4e inset and Figure 3h) were expected to withstand extreme deformation and impact damage.

Finite element method (FEM) was utilized to further analyze the tensile process of SHCF (Figure 4f). As a comparison, when the external stretch was only 16%, the FEM model of twisted hybrid conductive fiber produced an obvious first principal strain near the twisted necks at the longitudinal section due to the single extension of base material (right side in Figure 4f). The mises stress was also distributed at a high level throughout the section (right side in Figure S13, Supporting Information). Distinctively, stretch-induced strain was quite insensitive to the model of SHCF. The first principal strain increased marginally with the stretch ratio at 0%–400%, which was greatly undertaken by the structural deformation of coiled scaffold (left side in Figure 4f and Figure S14, Supporting Information). Even though the external stretch reached 500%, the strain and stress mainly focused on the inner circle of spiral section and still were below the highest level of that in twisted hybrid conductive fibers (Figure 4f and Figure S13, Supporting Information, middle).

Robust electrical stability over a broad deformation range was of paramount importance for stretchable conductors.^[36] Derived from the outstanding stretch-insensitive effect of

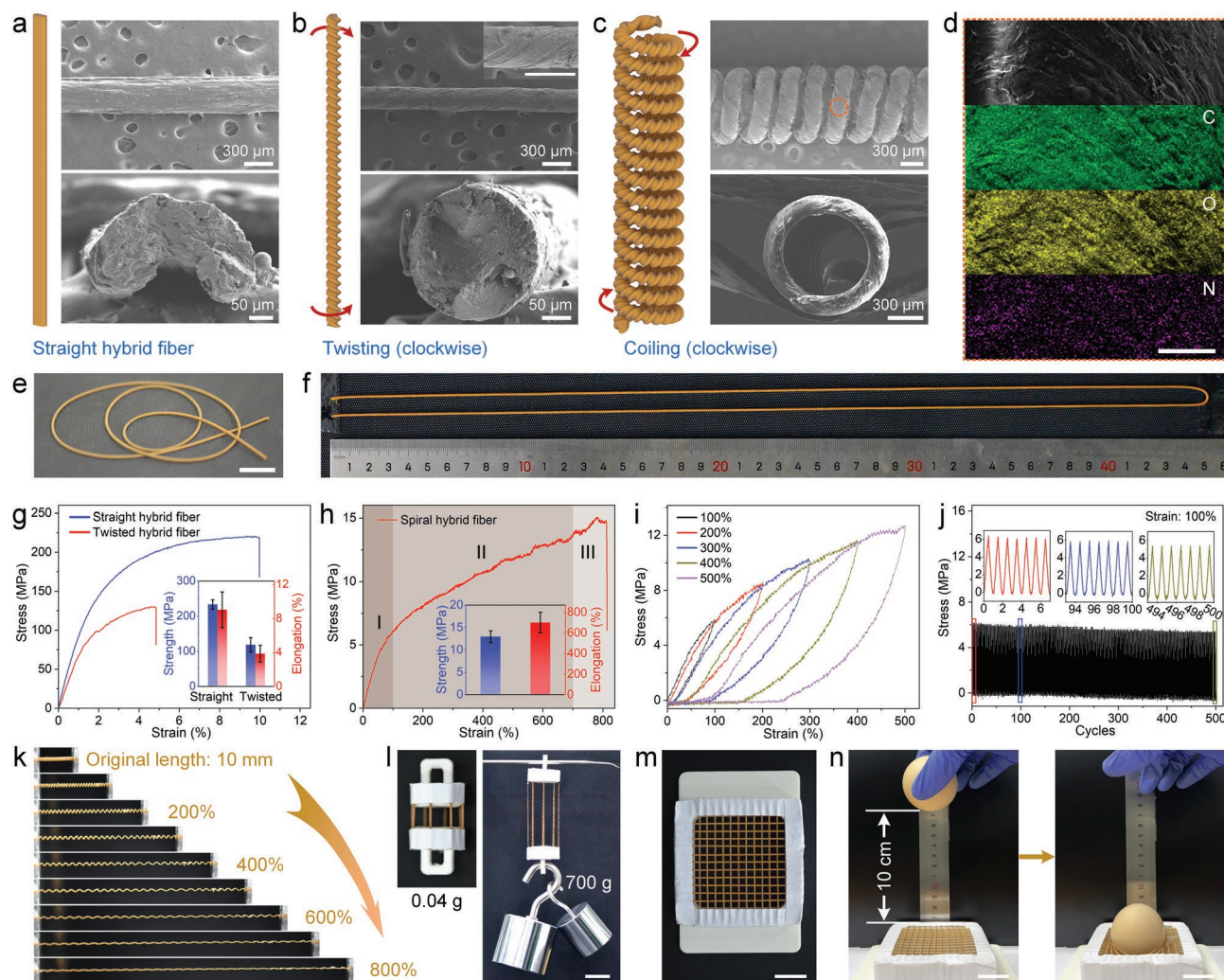


Figure 3. Structural characterization and mechanical performance of spiral hybrid fibers. Schematic diagrams and SEM images of a) straight hybrid fiber, b) twisted hybrid fiber (Inset represents the twisted structure. scale bar, 300 μm), and c) spiral hybrid fiber. d) EDS maps of the distributions of elemental carbon (C), oxygen (O), and nitrogen (N) in spiral hybrid fiber. Scale bar, 50 μm . Photographs of e) flexible spiral hybrid fiber and f) 90 cm long spiral hybrid fiber. Scale bar, 10 mm. Tensile stress-strain curves of g) straight hybrid fibers and twisted hybrid fibers, and h) spiral hybrid fibers. (Inset represents corresponding elongations and strengths) i) Consecutive loading-unloading of spiral hybrid fibers at strains of 100%, 200%, 300%, 400%, and 500%. j) 500 cyclic tensile tests of spiral hybrid fibers at strain of 100% and 0.25 Hz. k) Optical images of the stretch process of spiral hybrid fiber from original length to 800% strain. l) Photograph of spiral hybrid fibers sustaining 700 g weights. Scale bar, 20 mm. m) A elastic net with size of $6 \times 6 \text{ cm}^2$ woven by 22 spiral hybrid fibers. Scale bar, 20 mm. n) Snapshots of the buffer process of elastic net to a falling raw egg at 10 cm height. Scale bars, 20 mm. Error bars represent standard deviation.

SHCF, the variation in normalized resistance (R/R_0 , R and R_0 represented the resistances at stretched state and natural state respectively) was fairly unobvious as the tensile strain increased stepwise from 0% to 500% (Figure 4g). The maximum value of R/R_0 was only 1.02 ± 0.05 at 500% strain. It could be observed that the homochiral coiled structure unfolded significantly whereas the brightness of a connected LED hardly attenuated (Figure 4g insets), evidencing the highly effective coordination between conductivity and stretchability of SHCF. In addition, long-term electrical stability was another indispensable criterion for stretchable conductors. As presented in Figure 4h, the resistance almost remained constant during 5500 tensile cycles at 50% strain. When the strain increased to 100%, R/R_0 fluctuated moderately because of the slight tension of microfibrils.

But the maximum variation does not exceed $\pm 10\%$. Robust homochiral coiled structure was responsible for the exceptional fatigue-resistance. Figure S15, Supporting Information, further indicates the robust stability of coiled structure and AgNWs network after 5000 tensile cycles. Moreover, even being exposed to air for 90 days, the SHCFs exhibited tiny variations in R/R_0 (1.03 ± 0.03 , Figure 4i and Figure S16, Supporting Information), which reflected the long-term chemical stability of ANFs/PVA matrix and AgNWs coating in ambient environment.

For previous flexible conductors, various configurations (e.g., water-net structure, serpentine mesh circuit, buckled nanowire networks, and so on) have been proposed to construct highly conductive and stretchable matrices (Table S1, Supporting Information).^[9,37,38] However, the conductivity-stretchability

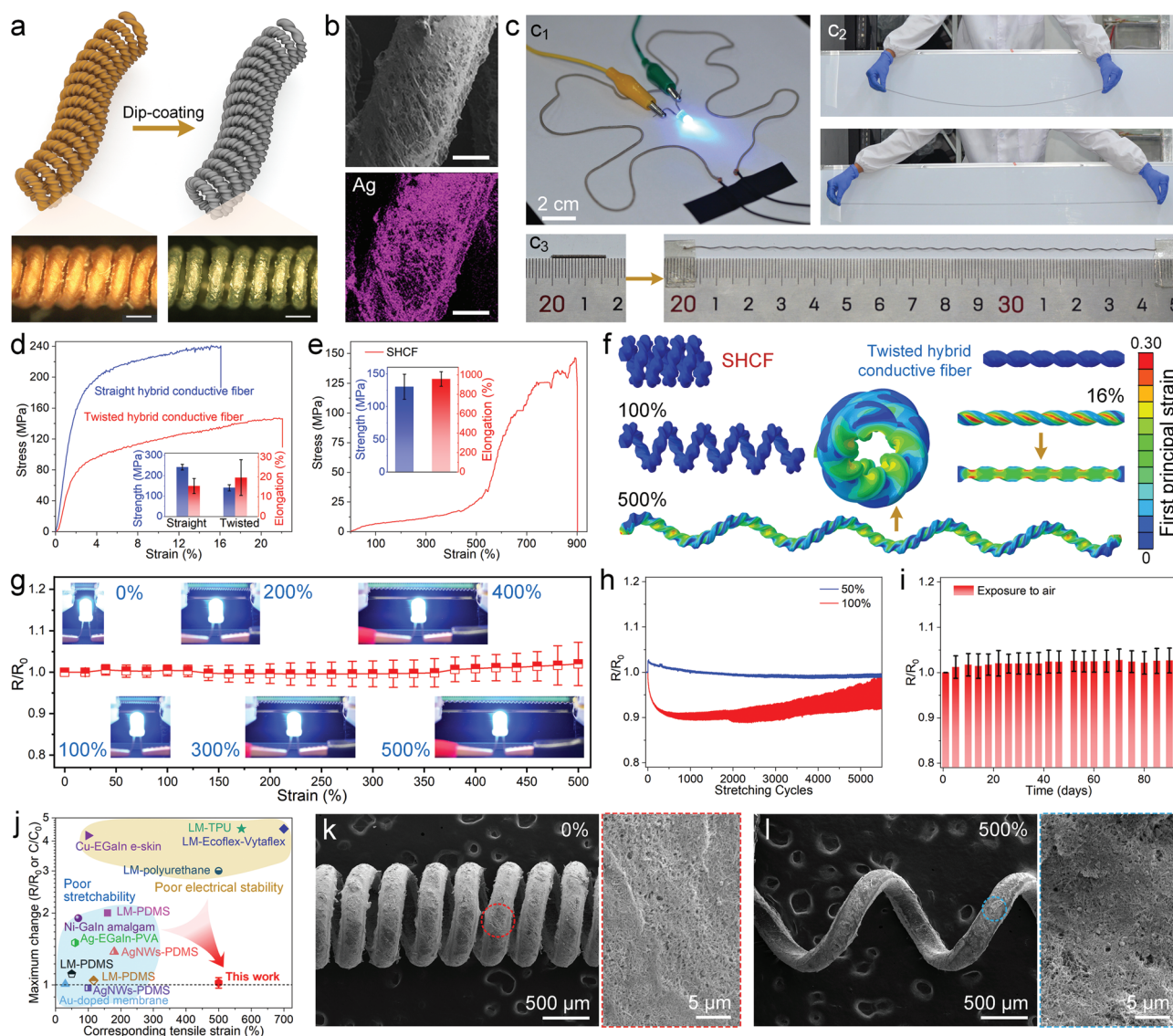


Figure 4. Mechanical and electrical performances of SHCF. a) Schematic illustration of the preparation of SHCF and corresponding optical micrographs. Scale bars, 500 μm . b) SEM image and EDS map of SHCF. Scale bars, 100 μm . c) Photographs of SHCFs with good conductivity (c₁), scalability (c₂), and extensibility (c₃). Tensile stress-strain curves of d) straight hybrid conductive fiber and twisted hybrid conductive fiber, and e) SHCF. (Inset represents corresponding elongations and strengths). f) Distributions of the first principal strain in uniaxial tensile FEM models of SHCF and twisted hybrid conductive fiber. g) The variation in normalized resistance of SHCF to tensile strain ranging from 0% to 500% (Insets represent the stretched sample that lighted up a blue LED). h) Variations in R/R_0 of SHCFs during 5500 tensile cycles at 50% and 100% strains. i) Variation in R/R_0 of SHCF exposed to air over time. j) Comparison of variation in R/R_0 (or C/C_0 , C denotes as capacitance) and corresponding tensile strain with previous stretchable conductors. SEM images of SHCFs at k) 0% strain and l) 500% strain (dashed boxes represent the densely deposited AgNWs). Error bars represent standard deviation.

dilemma yet remained intractable to resolve (Figure 4j), which was mainly caused by the severe deformation of electrical components during stretching. Benefiting from the robust homochiral coiled structure, SHCF in this work not only achieved ultrahigh elongation up to $958.2 \pm 75\%$, but also exhibited negligible electrical variation at 500% strain (1.02 ± 0.05 , Table S1, Supporting Information). To further visualize the stretch-insensitive effect, micro-morphologies of SHCFs at different stretch ratios were observed by SEM (Figure 4k,l and Figure S17, Supporting Information). Similar to the simulation results in Figure 4f, the spring geometries gradually expanded along with increased helical pitches from 0% to 500% strain, but these pro-

files of homochiral coiled fibers were almost consistent owing to the slight microfibrils tension. Deposited AgNWs stacked densely on these fiber surfaces as well, and no microcracks or slippages appeared at any stretch states (dotted boxes), thus maintaining a stable conductive path at large strain.

2.4. Demonstrations of Robust Electrical Stability of SHCF

Given the exceptional tensile property (Figure 4e), SHCF was capable of maintaining a steady output of electrical signals under extreme deformation conditions. For example, a

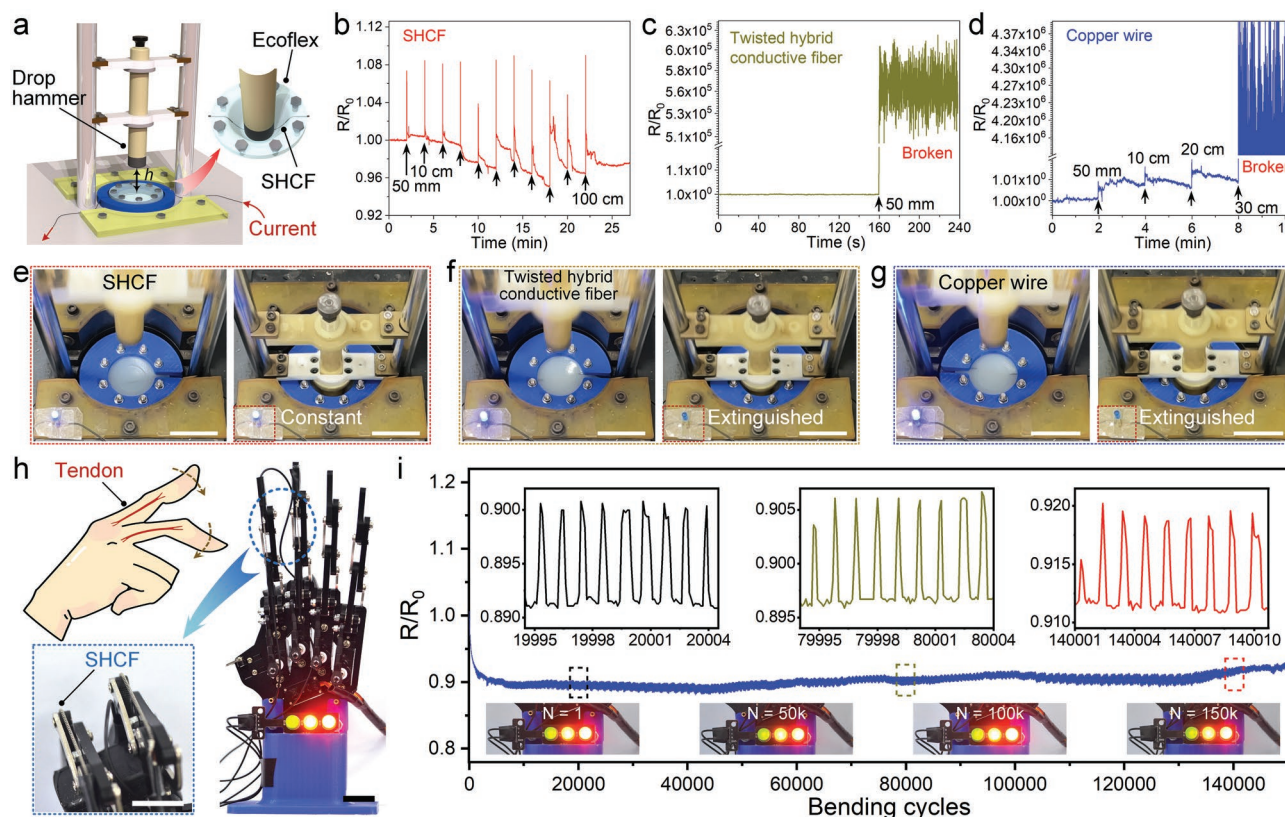


Figure 5. Electrical performances of SHCFs against impact damage and cyclic bending. a) Schematic illustration of the drop hammer impact process against Ecoflex embedded with SHCF. Variations in R/R_0 of b) SHCF, c) twisted hybrid conductive fiber, and d) copper wire to different impact heights. (Black arrows represent impact heights. Except for 50 mm, the height increased from 10 to 100 cm in steps of 10 cm.) Snapshots of the brightness changes of LEDs during impact processes (100 cm height) connected with e) SHCF, f) twisted hybrid conductive fiber, and g) copper wire, respectively. Scale bars, 50 mm. h) Schematic diagram of flexor tendons of human fingers and photographs of SHCFs attached on the bendable robotic fingers. Scale bars, 20 mm. i) Variation in R/R_0 of SHCF during cyclic bending of robotic finger (Insets represent the brightness change of LED over 150 000 cycles).

high-speed impact demonstration was conducted to evaluate the electrical stability of SHCF, in which a hammer (0.35 kg) was released from specific height (h) and fell onto the surface of an Ecoflex (Figure 5a). SHCF was embedded in this Ecoflex and then fixed by bolts (Figure S18, Supporting Information). As shown in Figure 5b, black arrows represented the electrical responses of the sample to various impact heights from 50 mm to 100 cm, where R/R_0 increased instantaneously at the moment of impact and then rapidly recovered after rebound. Interestingly, the variations were tiny during the whole process, showing the favorable robustness of SHCF under impactation. Despite the height reaching 100 cm, in which Ecoflex generated severe depression and high deformation rate within 10 ms (Figure S19, Supporting Information), the maximum value of R/R_0 was only 1.09, validating the remarkable electrical stability of SHCF against impact damage. For comparison, the same impact tests were performed on twisted hybrid conductive fiber and commercial copper wire, respectively (Figure S18b, Supporting Information). However, due to the low elongation (Figure 4d), twisted hybrid conductive fiber broke at an initial height of 50 mm as the resistance rose to infinity without decay (Figure 5c). As for commercial copper wire, although the R/R_0 increased slightly with height, it also could not withstand the impact damage at 30 cm height (Figure 5d). To compare the

impact stability more intuitively, LEDs were connected to these three samples respectively and supplied by a 3 V power source. The brightness changes of LEDs during test were recorded using high-speed camera. As shown in Figure 5e–g and Movie S3, Supporting Information, the hammer dropped from 100 cm height causing obvious depression and violent shock for all samples. Both twisted hybrid conductive fiber and copper wire were fractured as the LEDs extinguished immediately after impact. In sharp contrast, the robust homochiral coiled structure provided enough deformation space for SHCF to hold the constant brightness of LED during the multiple impact-rebound processes (Movie S3, Supporting Information). Such a comparison indicated superior electrical stability against the impact shock of SHCF than traditional metal conductive wires.

Flexor tendons of human fingers could keep powerful elasticity even after tens of thousands of joint bending. It was speculated that the SHCF possessed stable conductivity toward long-term fatigue tests like human tendons. Herein, a robotic hand was employed to demonstrate the fatigue-resistance of SHCF. As depicted in Figure 5h, they were attached to the finger joints and underwent tensile deformation during the finger bending process. Different bending radii were tested, including ≈ 70 , ≈ 63 , ≈ 40 , and ≈ 30 mm (Figure S20a, Supporting Information). When the bending radius decreased from ≈ 70 to ≈ 30 mm

successively, R/R_0 kept a similar change trend. The maximum variation was also no more than 1.008, reflecting the exceptional electrical stability against large bending degrees. Furthermore, the minimum bending radius of ≈ 30 mm was used to conduct the repeat bending action at a frequency of 1 Hz. The variation in conductivity was evaluated by the changes in LED brightness and measured resistance. It could be found that the R/R_0 declined to 0.9 at the initial 5000 cycles due to mild stretch of microfibrils and then fluctuated around this value all the time until 150 000 cycles (over 41 h, Figure 5i). The LED maintained invariant brightness throughout the lengthy fatigue test as well (Figure 5i insets and Movie S4, Supporting Information). Even though the coiled structures of SHCFs generated residual deformation during bending process, they almost recovered to their original morphologies slowly when the cycle was over (Figure S21, Supporting Information). These results implied the robust elasticity and durable stability of SHCF against cyclic deformation, which ensured their feasible application in long-term electrical transmission.

2.5. Highly Linear and Strain-Insensitive Temperature Perception of SHCF

Interestingly, besides the high electrical robustness against extreme deformation, SHCF exhibited excellent sensing capacity to environment temperature. As shown in Figure 6a, R/R_0 of SHCF possessed nearly synchronous variation with test temperature as it stepwise dropped from 100 to -20 °C. Linear voltage sweeps further reflected the temperature-dependent ohmic property of SHCF under the whole sensing range (Figure 6b). A similar electrical response to temperature was also found in twisted hybrid conductive fiber (Figure S22, Supporting Information), implying that the thermosensation of these fibers may result from the morphology change of deposited AgNWs. In order to investigate the response mechanism intuitively, atomic force microscopy (AFM) was utilized to analyze the stack status of AgNWs at different temperatures. The AgNWs that could be observed from the AFM images (Figure 6c, bottom side) gradually increased with temperature. Corresponding height distribution histograms (Figure S23, Supporting Information) further revealed that the roughness (R_q) of AgNWs decreased from 71.4 nm at 25 °C to 35.7 nm at 80 °C. This phenomenon appeared in twisted hybrid conductive fibers as well (Figure S24, Supporting Information). It indicated that AgNWs stacked more compactly on fiber surface at high temperatures so that the height differences among them were reduced. The densification process was probably caused by the thermal expansion of fiber matrix (Figure 6c, top side). Initially, AgNWs stacked loosely with high roughness at 25 °C, like well-dispersed building scaffolds accompanied with massive lap points (Figure 6c(I), red points in blue dotted boxes). These crosslinks among AgNWs formed a highly conductive path and macroscopically led to the low resistance of SHCF. When the test temperature increased to 60 °C, thermal expansion of fiber matrix perpendicular to stack direction tended to stretch the whole AgNWs scaffolds.^[39] The scattered and sank scaffolds further decreased the surface roughness (Figure 6c(II)). Meanwhile, partial lap points were eliminated due to the mutual

deviation of original crosslink sites, thereby reducing the conductivity of SHCF. At 80 °C, severe expansion of fiber matrix divided AgNWs into several parts with higher densification and caused lower surface roughness (Figure 6c(III)). The sparse crosslink sites between these parts contributed to the high electrical resistance of SHCF.

Based on this mechanism, SHCF was capable of withstanding long-term cyclic loading. In Figure 6d, when the test environment was circularly heated and cooled from 25 °C, namely 25 to -8 °C and 25 to 60 °C, R/R_0 showed identical change with temperature throughout the 23 cycles up to 300 min. The remarkable recoverability and durability could ensure the feasible operation of SHCF in extreme temperatures. In addition, response to tiny thermal fluctuations was crucial in precision measurement. It was found that SHCF exhibited a minimum resolution of ± 0.2 °C during the marginal heating and cooling process (Figure 6e and Figure S25a, Supporting Information). They could also accurately discriminate various temperature increments from ± 0.5 to ± 2 °C (Figure S25b, Supporting Information). Even with exposure to extreme environments (-10 , 60, and 90 °C), SHCF retained high monitoring precision to the slight temperature variations (Figure 6f). In comparison to reported temperature sensing electronics, such as thermosensitive hydrogels or metallic encapsulated circuits,^[40–42] the SHCF achieved simultaneously ultra-broad perception range and high resolution (Figure 6g and Table S2, Supporting Information), which were expected to detect diverse temperature variations from human bodies, liquids, and thermal instruments.

Through fitting the experimental data in Figure 6a, the electrical response of SHCF presented a highly linear relationship (correlation coefficient, $R^2 = 0.9998$) with temperature over the broad sensing range (Figure 6h). The calibration expression could follow $R/R_0 = 0.00227 \times T + 0.94245$ (T denoted as test temperature). To verify the utility of this relationship, both SHCF and commercial metal thermometers were fixed onto a slide attached to a temperature-controlled stage to monitor the identical heating-cooling process (Figure 6i, schematic). The stage was adjusted to -27 , 40, 60, 80, and 100 °C respectively from room temperature. As presented in Figure 6i and Figure S26, Supporting Information, all the temperature curves (red color) converted from electrical signals of SHCF maintained good synchronism with thermometer. Moreover, as the SHCF approached the front and back of a hand in turn, it could detect the subtle difference between room temperature and human body (Figure 6j). The temperature curve of SHCF (red line) even exhibited faster response time and more sensitive variation than thermometer when nearing the hand. Therefore, unlike most sensors with exponential or multi-regions linear characteristics,^[43,44] the linear response toward the broad sensing range of SHCF enabled expeditious temperature analysis without complex signal processing.

On account of the strain-insensitive electrical stability of SHCF (Figure 4g), it was deduced that large tensile deformation had little effect on the thermal-induced stack densification of AgNWs (Figure 6k). For that, SHCFs were stretched to 100%, 300%, and 500% strains respectively, and then subjected to the same temperature change as unstretched state. All the electrical responses presented in Figure 6l,m and Figure S27, Supporting Information, manifested nearly consistent variation

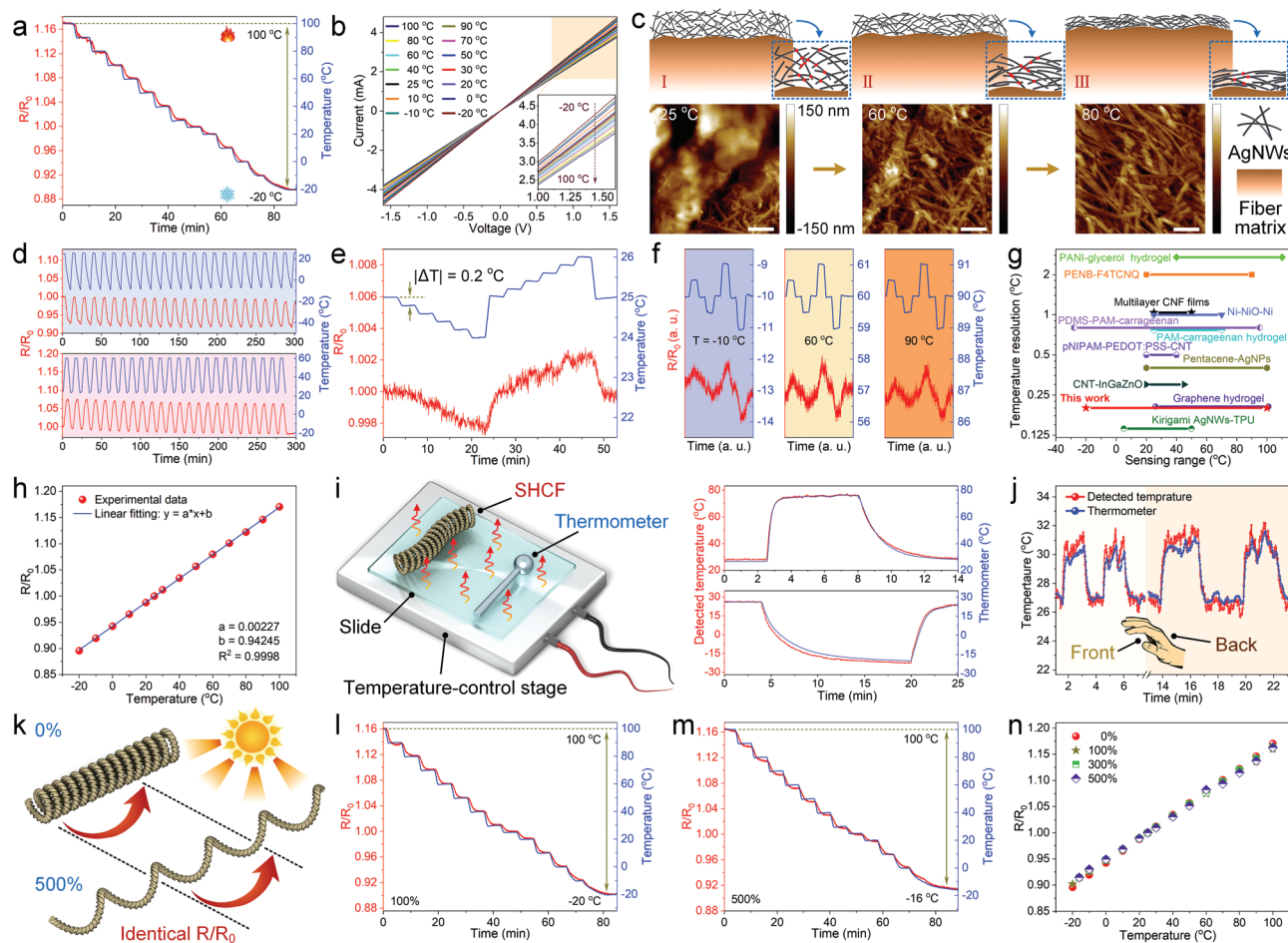


Figure 6. Temperature perception property of SHCF. a) R/R_0 of SHCF and test temperature as a function of time. b) Current-voltage curves of SHCF at different temperatures. c) Schematic illustration of the proposed temperature sensing mechanism (top) and AFM images of deposited AgNWs on SHCF at different temperatures (bottom). All color bars have the same height range. Scale bars, 1 μm . d) Variations in R/R_0 to cyclic heating process (25 to 60 $^{\circ}\text{C}$) and cooling process (25 to -8 $^{\circ}\text{C}$). e) Variation in R/R_0 to temperature around 25 $^{\circ}\text{C}$. The temperature changed in steps of 0.2 $^{\circ}\text{C}$. f) Responses of R/R_0 to tiny temperature changes at -10 , 60, and 90 $^{\circ}\text{C}$ respectively. g) Comparison of minimum resolution and sensing range of SHCF with existing temperature sensors. h) Linear fitting of the temperature sensing data of SHCF. i) Schematic diagram of temperature-control stage (left side) and temperature curves measured by SHCF and commercial thermometer respectively (right side). j) Temperature variations measured by SHCF (red line) and thermometer (blue line) as they approached the front and back of human hand. k) Schematic illustration of the strain-insensitive temperature perception feature. Temperature sensing curves of SHCFs at l) 100% strain and m) 500% strain. n) Variations in R/R_0 of SHCFs to test temperature at 0%, 100%, 300%, and 500% strains.

to temperature. Through integrating these experimental data, it could be seen that the sensitivity of SHCF was almost unchanged from 0% to 500% strain (Figure 6n). Notably, the large-deformation-insensitive temperature perception surpassed most existing sensors with moderate strain tolerance (below 100%),^[14,37] allowing for convenient measurement of amorphous objects.

2.6. Liquid Temperature Perception in Multiple Occasions

Benefiting from the portable spring morphology, SHCFs could be cut into arbitrary lengths and assembled into an array system. Herein, a 5×5 sensor array was fabricated to acquire the spatial distribution of hot/cold objects (Figure 7a). Four water containers with different liquid temperatures (“U” at ≈ 71 $^{\circ}\text{C}$,

“S” at ≈ 66 $^{\circ}\text{C}$, “T” at ≈ 54 $^{\circ}\text{C}$, and “C” at ≈ -21 $^{\circ}\text{C}$, Figure S28, Supporting Information) were respectively placed above the array with 5 mm spacing. Through capturing the thermal diffusion generated by these containers, the sensor array displayed highly consistent color heat maps with thermographic images (Figure 7b and Figure S28, Supporting Information). Besides, the color bars manifested different variations in R/R_0 to various water temperatures from 71 to -21 $^{\circ}\text{C}$. For example, the “U”-shaped water container at ≈ -10 $^{\circ}\text{C}$ induced negative resistance change of array compared to the “U” at ≈ 71 $^{\circ}\text{C}$, whose variation degree was slighter than “C” at ≈ -21 $^{\circ}\text{C}$ (Figure 7b and Figure S29, Supporting Information). As a result, the accurate differentiation to spatial profile and temperature of hot/cold objects was reminiscent of the advanced sensing system on human skin, which held promise for integrated perception in complex thermal fields.

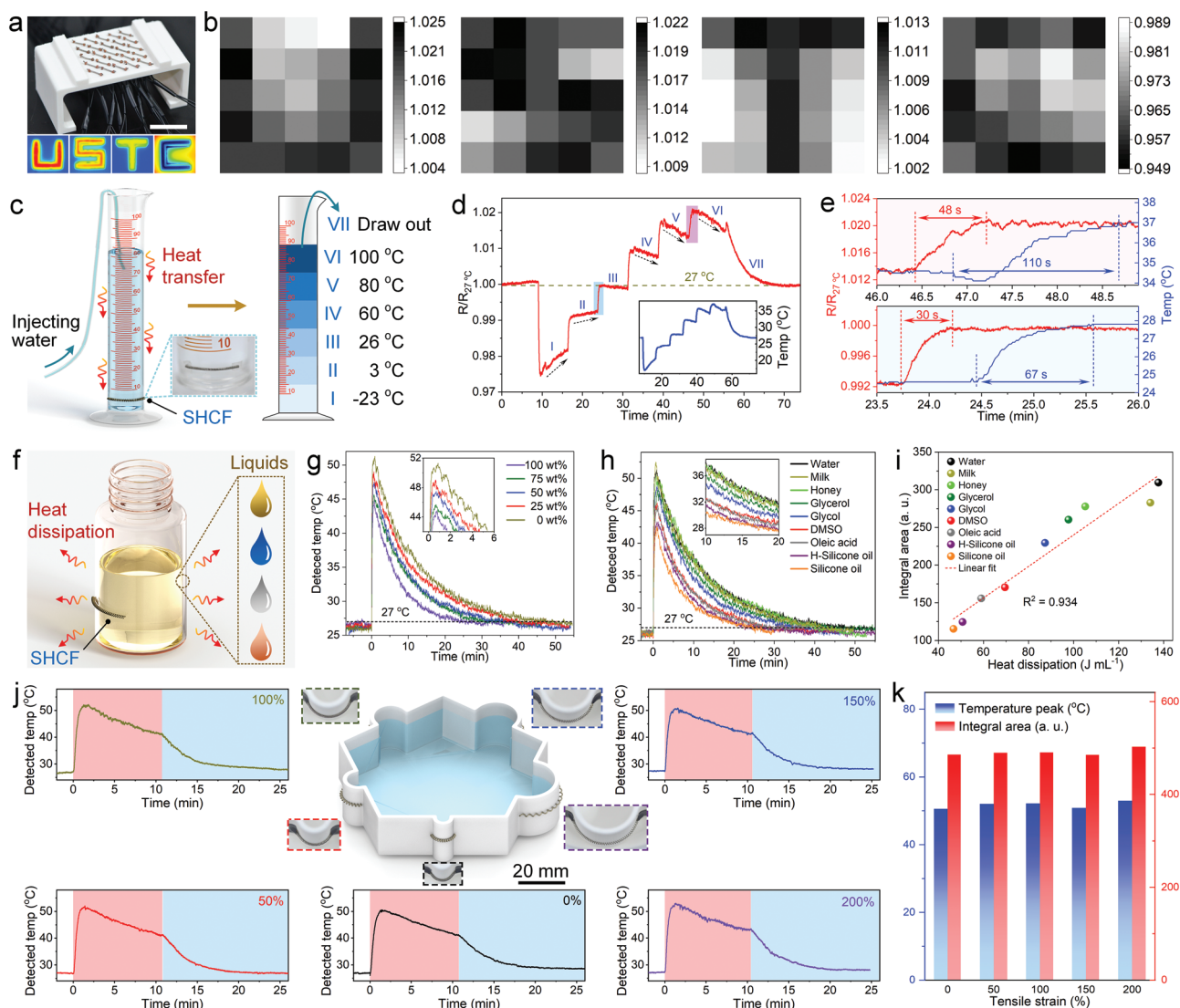


Figure 7. Demonstration of liquid temperature monitoring of SHCF. a) Photograph of 5×5 temperature sensor array based on SHCF (top) and thermographic images of letter-like water containers (bottom). Scale bar, 30 mm. b) Color heat maps of letter patterns (“U”, “S”, “T”, and “C”) detected by sensor array. The color bars represent the changes of R/R_0 . c) Schematic illustration of the temperature detection of SHCF to various liquids in graduated cylinder. d) Normalized resistance change of SHCF to injected liquids with different temperatures from -23 to 100 °C. Inset represents the real-time temperature measured by thermometer. e) Comparisons of response times between SHCF (red curve) and thermometer (blue curve) at stage V→VI (pink area) and II→III (blue area). f) Schematic illustration of the temperature monitoring of SHCF to heat dissipation of various liquids. g) Temperatures measured by SHCF to the aqueous solutions with different ethanol contents. h) Temperature curves measured by SHCF to various liquids and i) their integral areas as a function of theoretical heat dissipation. j) Water temperature changes measured by SHCFs at different tensile strains (0%–200%). The red and blue regions in the figures represent natural cooling and cooling after water extraction, respectively. Schematic and photographs of the water container with different circular profiles. k) Corresponding peak values and integral areas at red regions of temperature curves.

Real-time detection of water temperature was helpful to analyze the thermal diffusion that occurred in liquid environment. As depicted in the left side of Figure 7c, SHCF was used to monitor the temperature change driven by heat transfer among various liquids. Specifically, liquids including ethanol (-23 °C) and water (3, 26, 60, 80, and 100 °C) were sequentially injected into a graduated cylinder every ≈ 7 min in the same volume of 15 mL (right side in Figure 7c). The monitored electrical signal mainly consisted of transient variation phases and long platform stages, which represented the rapid liquid injection and slow temperature balance, respectively (Figure 7d). Since the

heat diffused down to the bottom of graduated cylinder by thermal conduction and convection, R/R_0 of the platform stages improved gradually from I to VI. The oblique black arrows further indicated that the higher the temperature of added liquid, the faster the cooling speed, implying the precise perception to heat transfer among various temperatures. In the meanwhile, the temperature curve measured by metal thermometer validated the feasible electrical signal of SHCF (Figure 7d inset). Owing to the good flexibility, SHCF possessed fast response speed after water injection through conformal contact with the curved wall of graduated cylinder. For example, the time

intervals from V to VI (pink area, 48 s) and II to III (blue area, 30 s) were less than half of that of rigid metal thermometers (110 and 67 s, Figure 7e). Finally, the R/R_0 returned to initial level slowly after the mixed liquids were drawn out at stage VII (Figure 7d).

Based on the conformal attachment, feasible monitoring, and fast response, the SHCF could be further applied to differentiate the type and content of liquids through assessing their heat dissipation properties. Herein, aqueous solutions (9 mL) with different ethanol contents (0, 25, 50, 75, and 100 wt.%) were heated to 60 °C and then injected into a glass bottle placed at room temperature (Figure 7f). The thermal dissipation-induced cooling processes were detected by SHCF (Figure 7g). All temperature curves elevated drastically at the initial phase and then descended slowly in an exponential manner. However, the addition of ethanol tended to increase the thermal conductivity and lower the heat capacity of aqueous solutions, thus enhancing the heat dissipation rate.^[43] With the increase of ethanol content, the temperature peaks gradually dropped from 51 to 45 °C (Figure 7g inset). The cooling times also shortened from 48 to 25 min (Figure S30, Supporting Information), indicating the exact perception of thermophysical properties of liquids. Subsequently, more liquids including milk, honey, glycerol, glycol, DMSO, oleic acid, H-silicone oil (“H” represented “hydroxy”), and silicone oil, were employed to undergo the same cooling process. The monitored temperatures showed a similar variation tendency to ethanol aqueous solutions but with diverse cooling rates (Figure 7h). Generally, the dissipated heat quantities of liquids could be acquired by integrating the temperature curves over cooling time (Figure S31, Supporting Information), which were positively correlated to the volume-specific heat capacity. As shown in Figure 7i, the integral area manifested a favorable linear relationship with the theoretical heat dissipation, corroborating the extraordinary thermal analysis capacity of various liquids of SHCF.

Flexibility and robustness were considered as crucial design factors in modern electronics. However, most existing sensing devices faced the fatal deficiency of deformation failure when suffering extreme tension or compression. It was worth noting that the strain-independent sensitivity (Figure 6n) allowed SHCF to monitor temperature at a highly stretched state. The schematic in Figure 7j illustrated its practical utility in the heat dissipation analysis of hot water at 60 °C. To real-time detect the cooling process at multiple positions, five SHCFs of the same length were attached to corresponding circular surfaces of the water container, thus generating different tensile strains (photographs in dashed boxes). It could be observed that the measured temperature curves maintained almost identical tendencies from 0% to 200% strain (Figure 7j). Figure 7k and Figure S32, Supporting Information, summarized the temperature peaks and integral areas at red regions of these five conditions. Compared to unstretched state, their maximum deviations only were 4.7% (temperature peaks) and 3.5% (integral areas) respectively, suggesting the stable sensing capacity toward a broad strain range. Such an outstanding deformation-tolerance of SHCF could achieve flexible temperature monitoring of objects with complex profiles.

3. Conclusion

In summary, an ultra-stretchable SHCF was devised that combined strain-insensitive electrical stability and temperature perception. Inspired by cucumber tendrils, the homochiral coiled configuration of SHCF delivered maximum elongation of 958% through retarding stretch-induced deformation of fiber matrix. The gentle uncoiled motion further endowed it with negligible resistance variation against extreme tensile strain (500%). Multiple stimuli, including high-speed impact damage, air exposure for 90 days, and cyclic bending for 150 000 times, demonstrated the extraordinary robustness and resilience of SHCF that outperformed other stretchable conductors. Benefiting from the thermal-induced stack densification of AgNWs, the SHCF was proven to show precise perception of environment temperature in a wide range (−20 to 100 °C). Its highly linear response achieved expeditious thermal analysis of the heat dissipation properties of various liquids. Interestingly, the sensing capacity could be well maintained even at a high tensile state of 500% strain, thus enabling convenient temperature measurement for irregular surfaces by conformal contact. Overall, the highly deformation-tolerant electrical performances demonstrated the ingenious configuration design of SHCF, which possessed great potential to develop wearable electronics, stretchable artificial tendons, and thermal field monitoring.

4. Experimental Section

Materials: Para-aramid fabrics were supplied by Junantai Co., Ltd. Polyvinyl alcohol powder (PVA-124, viscosity: 54–66 mPa s) was purchased from Sigma-Aldrich Inc. Dimethyl sulfoxide (DMSO), polyvinyl pyrrolidone (PVP), silver nitrate (AgNO₃), sodium chloride (NaCl), potassium hydroxide (KOH), glycerol, and ethanol were obtained from Sinopharm Chemical Reagent Co., Ltd.

Preparation of ANFs/PVA/DMSO Dispersion: Para-aramid fabrics and PVA were dissolved in DMSO respectively to acquire ANFs (2 wt.%) and PVA (10 wt.%) dispersions according to previous reports.^[19,26] Then, they were mixed with each other in a mass ratio of 1:1. After stirring at 73 °C for a week, the ANFs/PVA/DMSO dispersion was obtained.

Wet-Spinning of ANFs/PVA Hydrogel Yarns: 25 mL of ANFs/PVA/DMSO mixture was sucked into a syringe and heated at 65 °C using a heat jacket. The mixture was extruded into an oil bath (dimethyl silicone oil, 5 °C) through a round needle (18 G) with a speed of 2 mL min^{−1}, which formed spinning yarns in the oil bath. The yarns were then wrapped and drawn using two synchronously rotating rollers with a diameter ratio of 1:4. During the draw process, the yarns gelled gradually in deionized (DI) water (Figure 2c). Finally, the obtained ANFs/PVA hydrogel yarns were washed to remove residual oil and preserved in fresh DI water.

Preparation of Spiral Hybrid Fibers: Two ends of ANFs/PVA hydrogel yarn with specific lengths were tethered to a rotator head and a round mandrel (Φ 0.7 mm), respectively. Followed by fixing the mandrel to straighten the yarn, rotator head was twisted along the central axis of yarn at 300 rpm with a given twisted density of 1500 turns m^{−1}. The obtained twisted hybrid fiber was then coiled around the mandrel and annealed at 100 °C for 3 h to set the spiral shape. Note that the twisting and coiling directions were the same (clockwise) to acquire a homochiral structure.

Preparation of SHCFs: First, AgNWs were fabricated according to previous method.^[45] In a brief, 5.86 g PVP was dissolved completely in 190 mL glycerol by stirring at 80 °C. 1.58 g AgNO₃ along with a mixture containing NaCl (0.059 g), DI water (0.2 mL), and glycerol (10 mL) were then added to the solution. The stirring was kept at 210 °C for 20 min

until the solution turned into gray-green. Followed by standing at room temperature for a week, the precipitation in solution was extracted by centrifuging at 7500 rpm and washed with DI water and ethanol successively for three times. The obtained AgNWs were preserved in 75 mL ethanol. Then, spiral hybrid fibers were dipped in the prepared AgNWs/ethanol dispersion for 5 min. After sufficient deposition of AgNWs, the fibers were dried at 60 °C for another 5 min to remove absorbed ethanol. The dipping-drying process was repeated for 10 times to obtain SHCFs.

Characterization and Test: The morphologies of sample fibers were observed by an SEM Gemini 500 (Carl Zeiss Jena, Germany). The orientation structures of hydrogel yarns were observed using a confocal microscope (Leica SP8, Germany). 0.1 wt.% fluorescein sodium aqueous was used to dye the hydrogel yarns and excited using a laser at 488 nm.^[33] Fourier Transform Infrared Spectra were characterized using an FTIR Nicolet 8700 (Thermo Nicolet, USA). The morphology changes of deposited AgNWs on fiber matrix at different temperatures were observed by AFM (DI Innova, Veeco, USA). Rheological behavior of ANFs/PVA/DMSO mixture was evaluated by a rheometer (MCR 302, Anton Paar, Austria) using a parallel plate (PP20, Φ 20 mm) with a gap size of 1 mm. The test temperature was raised from -10 to 95 °C by 3 °C min⁻¹. Tensile properties of sample fibers (gauge length, 10 mm) were tested using an ElectroForce 3320 (TA instruments) with a stretch rate of 5 mm min⁻¹. Electrical performance was measured by a ModuLab test system (Solartron Analytical, AMETEK).

Stretching Simulation: SHCF and twisted hybrid conductive fiber were simplified with homochiral coiled structure and twisted structure, respectively. These structures were constructed by solid elements using Finite Element Method (Abaqus/Statics), which were subjected to quasi-static stretch along fiber axis. An elastoplastic model with Poisson's ratio of 0.3 was used to describe the fiber materials. Corresponding mechanical parameters were extracted from the tensile curve of straight hybrid conductive fiber in Figure 4d. The Young's modulus and initial yield stress were set as 10.24 GPa and 147.52 MPa, respectively. True strain and true stress were calculated in every time step.

Supporting Information

Supporting Information is available from the Wiley Online Library or from the author.

Acknowledgements

This work was supported by the National Natural Science Foundation of China (grant nos. 12072338, 12132016, 11972032, 12102424, and 12202435), the China Postdoctoral Science Foundation (Grant No. 2021M703086), the Aviation Science Foundation of China (20200029079004), and the Fundamental Research Funds for the Central Universities (WK2480000007). The USTC Center for Micro- and Nanoscale Research and Fabrication also makes contribution in the microstructural characterization of spiral conductive fibers.

Conflict of Interest

The authors declare no conflict of interest.

Data Availability Statement

The data that support the findings of this study are available from the corresponding author upon reasonable request.

Keywords

deformation-independent sensitivity, electrical stability, homochiral coil, temperature perception, ultra-stretchable fibers

Received: November 29, 2022

Revised: February 2, 2023

Published online: February 17, 2023

- [1] D. Qi, Z. Liu, M. Yu, Y. Liu, Y. Tang, J. Lv, Y. Li, J. Wei, L. Bo, Z. Yu, X. Chen, *Adv. Mater.* **2015**, *27*, 3145.
- [2] X. Wang, K. Chan, W. Lu, T. Ding, S. Ng, Y. Cheng, T. Li, M. Hong, B. Tee, G. Ho, *Nat. Commun.* **2022**, *13*, 3369.
- [3] H. Zhou, J. Lai, B. Zheng, X. Jin, G. Zhao, H. Liu, W. Chen, A. Ma, X. Li, Y. Wu, *Adv. Funct. Mater.* **2022**, *32*, 2108423.
- [4] X. Yu, X. Gong, C. Podder, B. Ludwig, I. Chen, W. Shou, A. Alvidrez, G. Chen, X. Huang, H. Pan, *Adv. Eng. Mater.* **2021**, *23*, 2100286.
- [5] H. Jin, N. Matsuhisa, S. Lee, M. Abbas, T. Yokota, T. Someya, *Adv. Mater.* **2017**, *29*, 1605848.
- [6] X. Li, P. Zhu, S. Zhang, X. Wang, X. Luo, Z. Leng, H. Zhou, Z. Pan, Y. Mao, *ACS Nano* **2022**, *16*, 5909.
- [7] J. Lyu, M. Hammig, L. Liu, L. Xu, H. Chi, C. Uher, T. Li, N. Kotov, *Appl. Phys. Lett.* **2017**, *111*, 161901.
- [8] S. Wu, S. Yao, Y. Liu, X. Hu, H. Huang, Y. Zhu, *ACS Appl. Mater. Interfaces* **2020**, *12*, 41696.
- [9] J. Cao, F. Liang, H. Li, X. Li, Y. Fan, C. Hu, J. Yu, J. Xu, Y. M. Yin, F. Li, D. Xu, H. Feng, H. Yang, Y. Liu, X. Chen, G. Zhu, R. W. Li, *InfoMat* **2022**, *4*, e12302.
- [10] R. Guo, B. Cui, X. Zhao, M. Duan, X. Sun, R. Zhao, L. Sheng, J. Liu, J. Lu, *Mater. Horiz.* **2020**, *7*, 1845.
- [11] R. Zheng, Y. Wu, Y. Xu, S. Liu, H. Liu, P. Wang, Z. Deng, S. Chen, L. Liu, *Mater. Lett.* **2019**, *235*, 133.
- [12] J. Kim, M. Lee, H. Shim, R. Ghaffari, H. Cho, D. Son, Y. Jung, M. Soh, C. Choi, S. Jung, K. Chu, D. Jeon, S. Lee, J. Kim, S. Choi, T. Hyeon, D. Kim, *Nat. Commun.* **2014**, *5*, 5747.
- [13] K. Sim, Z. Rao, Z. Zou, F. Ershad, J. Lei, A. Thukral, J. Chen, Q. Huang, J. Xiao, C. Yu, *Sci. Adv.* **2019**, *5*, eaav9653.
- [14] Y. Yu, S. Peng, Z. Sha, T. Cheng, S. Wu, C. Wang, *J. Mater. Chem. A* **2021**, *9*, 24874.
- [15] Q. Guo, J. Dong, Y. Liu, X. Xu, Q. Qin, J. Wang, *Acta Mech. Sin.* **2019**, *35*, 702.
- [16] Y. Cui, D. Li, C. Gong, C. Chang, *ACS Nano* **2021**, *15*, 13712.
- [17] I. Must, E. Sinibaldi, B. Mazzolai, *Nat. Commun.* **2019**, *10*, 344.
- [18] Y. Gao, F. Guo, P. Cao, J. Liu, D. Li, J. Wu, N. Wang, Y. Su, Y. Zhao, *ACS Nano* **2020**, *14*, 3442.
- [19] M. Yang, K. Cao, L. Sui, Y. Qi, J. Zhu, A. Waas, E. Arruda, J. Kieffer, M. Thouless, N. Kotov, *ACS Nano* **2011**, *5*, 6945.
- [20] Y. Han, K. Ruan, J. Gu, *Angew. Chem.* **2023**, *62*, e202216093.
- [21] Z. Liu, J. Lyu, D. Fang, X. Zhang, *ACS Nano* **2019**, *13*, 5703.
- [22] Z. Zhang, S. Yang, P. Zhang, J. Zhang, G. Chen, X. Feng, *Nat. Commun.* **2019**, *10*, 2920.
- [23] C. Xie, L. He, Y. Shi, Z. Guo, T. Qiu, X. Tuo, *ACS Nano* **2019**, *13*, 7811.
- [24] Y. Zhang, Z. Ma, K. Ruan, J. Gu, *Research* **2022**, *2022*, 9780290.
- [25] X. Dong, X. Guo, Q. Liu, Y. Zhao, H. Qi, W. Zhai, *Adv. Funct. Mater.* **2022**, *32*, 2203610.
- [26] Y. Chen, Q. Zhang, Y. Zhong, P. Wei, X. Yu, J. Huang, J. Cai, *Adv. Funct. Mater.* **2021**, *31*, 2104368.
- [27] Z. Ma, X. Xiang, L. Shao, Y. Zhang, J. Gu, *Angew. Chem.* **2022**, *61*, e202200705.
- [28] Y. Han, K. Ruan, J. Gu, *Nano Res.* **2022**, *15*, 4747.
- [29] Y. Yang, J. Han, J. Huang, J. Sun, Z. Wang, S. Seo, Q. Sun, *Adv. Funct. Mater.* **2020**, *30*, 1909652.

- [30] H. He, X. Wei, B. Yang, H. Liu, M. Sun, Y. Li, A. Yan, C. Tang, Y. Lin, L. Xu, *Nat. Commun.* **2022**, *13*, 4242.
- [31] J. Zhu, M. Yang, A. Emre, J. Bahng, L. Xu, J. Yeom, B. Yeom, Y. Kim, K. Johnson, P. Green, N. Kotov, *Angew. Chem., Int. Ed.* **2017**, *56*, 11744.
- [32] Y. Guan, W. Li, Y. Zhang, Z. Shi, J. Tan, F. Wang, Y. Wang, *Compos. Sci. Technol.* **2017**, *144*, 193.
- [33] Z. Ma, Q. Huang, Q. Xu, Q. Zhuang, X. Zhao, Y. Yang, H. Qiu, Z. Yang, C. Wang, Y. Chai, Z. Zheng, *Nat. Mater.* **2021**, *20*, 859.
- [34] M. Kanik, S. Orguc, G. Varnavides, J. Kim, T. Benavides, D. Gonzalez, T. Akintilo, C. Tasan, A. Chandrakasan, Y. Fink, P. Anikeeva, *Science* **2019**, *365*, 145.
- [35] X. Liang, G. Chen, S. Lin, J. Zhang, L. Wang, P. Zhang, Z. Wang, Z. Wang, Y. Lan, Q. Ge, J. Liu, *Adv. Mater.* **2021**, *33*, 2102011.
- [36] Z. Yu, J. Shang, X. Niu, Y. Liu, G. Liu, P. Dhanapal, Y. Zheng, H. Yang, Y. Wu, Y. Zhou, Y. Wang, D. Tang, R. Li, *Adv. Electron. Mater.* **2018**, *4*, 1800137.
- [37] M. Sang, K. Kang, Y. Zhang, H. Zhang, K. Kim, M. Cho, J. Shin, J. Hong, T. Kim, S. Lee, W. Yeo, J. Lee, T. Lee, B. Xu, K. J. Yu, *Adv. Mater.* **2022**, *34*, 2105865.
- [38] B. Kim, H. Kwon, H. Kwon, J. Pyo, J. Oh, S. Hong, J. Park, K. Char, J. Ha, J. Son, S. Lee, *Adv. Funct. Mater.* **2020**, *30*, 1910214.
- [39] Y. Gotoh, Y. Nagara, T. Nakano, Y. Okamoto, Y. Ohkoshi, M. Nagura, *J. Polym. Sci., Part B: Polym. Phys.* **2004**, *42*, 800.
- [40] G. Ge, Y. Lu, X. Qu, W. Zhao, Y. Ren, W. Wang, Q. Wang, W. Huang, X. Dong, *ACS Nano* **2020**, *14*, 218.
- [41] J. Shin, B. Jeong, J. Kim, V. Nam, Y. Yoon, J. Jung, S. Hong, H. Lee, H. Eom, J. Yeo, J. Choi, D. Lee, S. Ko, *Adv. Mater.* **2020**, *32*, 1905527.
- [42] X. Ren, K. Pei, B. Peng, Z. Zhang, Z. Wang, X. Wang, P. Chan, *Adv. Mater.* **2016**, *28*, 4832.
- [43] Y. Lee, J. Park, A. Choe, Y. Shin, J. Kim, J. Myoung, S. Lee, Y. Lee, Y. Kim, S. Yi, J. Nam, J. Seo, H. Ko, *ACS Nano* **2022**, *16*, 1208.
- [44] J. Ngai, J. Polena, D. Afzal, X. Gao, M. Kapadia, Y. Li, *Adv. Funct. Mater.* **2022**, *32*, 2110995.
- [45] C. Yang, H. Gu, W. Lin, M. Yuen, C. Wong, M. Xiong, B. Gao, *Adv. Mater.* **2011**, *23*, 3052.